Eur Biophys J (2010) 39:861–865
DOI 10.1007/s00249-009-0541-y

BIOPHYSICS LETTER

Synchrotron X-ray imaging via ultra-small-angle scattering: principles of quantitative analysis and application in studying bone integration to synthetic grafting materials

Sérgio L. Morelhão · Paulo G. Coelho · Marcelo G. Hönnicke

Received: 6 May 2009 / Revised: 2 July 2009 / Accepted: 8 September 2009 / Published online: 27 September 2009

Abstract Optimized experimental conditions for extracting accurate information at subpixel length scales from analyzer-based X-ray imaging were obtained and applied to investigate bone regeneration by means of synthetic β-TCP grafting materials in a rat calvaria model. The results showed a 30% growth in the particulate size due to bone ongrowth/ingrowth within the critical size defect over a 1-month healing period.

Keywords Synchrotron · Ultra-small-angle scattering · Bone · Grafting material · In vivo

Phase contrast X-ray imaging (Wilkins et al. 1996; Davis et al. 1995; Pfeifer et al. 2006; Hönnicke et al. 2008) is a well-established tool to present details of biological tissues that are invisible or indistinguishable by conventional radiography. Its applications have been evaluated in many scientific fields and with a variety of phase-sensitive techniques (Westneat et al. 2003; Antunes et al. 2006; Wagner et al. 2006). Analyzer-based imaging (ABI) (Davis et al. 1995; Foerster et al. 1980) is sensitive to the phase gradient due to refraction. However, in contrast to the other techniques, ABI is also capable of providing information on two other major radiation-matter interaction processes: photoelectric absorption and small-angle scattering (Bonse and Hart 1966). Although refraction is the contrast mechanism able to resolve features on the length scale of the spatial resolution of detector systems, typically on the order of some tens of microns, small-angle scattering is the process that is sensitive to density fluctuation on shorter scales of a few microns or less. Extensively exploited to probe low ordered systems, such as macro molecules in solution, small-angle scattering techniques are one of the most fundamental X-ray tools for the microstructure characterization of solid and fluid materials (Glatter and Kratky 1982). In spite of its short-scale probing potential, small-angle scattering as an imaging contrast mechanism, where it is commonly called ultra-small-angle X-ray scattering (USAXS), has been treated marginally qualitatively in a few cases (Antunes et al. 2006; Levine and Long 2004; Muehleman et al. 2006). In most cases, it is treated as a sub-product owing to an undesired process that can smear fine structural details of the refraction images (Coan et al. 2008; Zhong et al. 2000; Pisano et al. 2000; Pagot et al. 2003; Rigon et al. 2007).

In medicine, biology, and related fields, the usage of USAXS images to locate and characterize distinct distributions of microscopic alterations over vast tissues (centimeter scale) opens a wide range of opportunities. For instance, USAXS can be used in studying multifactorial diseases with large ensembles of clinical cases, as in the study of cataract where USAXS images could easily evaluate microcalcifications over entire eye lenses (Antunes et al. 2006). Evaluation of osteoporosis, osteoarthritis (Coan et al. 2008), and implant-bone integration (Wagner et al. 2006) are other examples of studies that can be enriched by

S. L. Morelhão
Instituto de Física, Universidade de São Paulo,
São Paulo, SP, Brazil
e-mail: morelhao@if.usp.br

P. G. Coelho (✉)
Department of Biomaterials and Biomimetics,
New York University, New York, NY, USA
e-mail: pgcoelho@nyu.edu

M. G. Hönnicke
NSLS II, Brookhaven National Laboratory,
Upton, NY 11973, USA
e-mail: mhonnicke@bnl.gov

USAXS imaging. Although some of its potential for investigating biological tissues has already been recognized (Muehleman et al. 2006), the actual state of the art of USAXS imaging only allows distinguishing microstructured tissue from homogeneous tissue without providing accurate information on the microscale density fluctuations. To achieve its full potential as a general imaging resource, it is fundamental to develop data analysis procedures capable of determining the accuracy by which the length scale of the density fluctuation on a subpixel resolution can be retrieved. In this work, one such procedure is developed for cases in which USAXS arises from a coherent scattering process. The procedure is first used to verify the spatial resolution achieved by a few ABI setups. Then, by employing the setup configuration that provides the best resolution, the feasibility of extracting accurate microscale information is demonstrated in the present study concerning bone integration to a biocompatible material widely used in dental and medical applications.

Form and function replacement of lost hard tissue through guided regeneration by means of synthetic materials or tissue engineering (tissue regeneration at cellular level) has been of interest to both healthcare practitioners and patients. The reason for such interest includes avoiding a second surgical site and procedure, i.e., autologous bone grafting, and the potential secondary infection due to cadaveric (allogenous) and animal (xenogenous) bone processing for grafting purposes (LeGeros 1991; Lemons 1996). Among bioceramics, Ca- and P-based synthetic materials such as hydroxyapatite, β-tricalcium phosphate (β-TCP), or $Ca_3(PO_4)_2$, and biphasic blends have been widely utilized in dentistry and orthopedics (LeGeros 1991). These materials have been employed as bone defect filling materials, implant coatings, bone substitutes, drug delivery/biologic carriers, and resorbable scaffolds (Lemons 1996). These various applications originated due to their degradation followed by bone replacement as time elapses in vivo (LeGeros 1991; Lemons 1996). In the present study, artificial bone regeneration by means of synthetic β-TCP grafting materials in a rat calvaria model was investigated by spatially resolved USAXS images.

Before starting our theoretical treatment, it is worth emphasizing that USAXS can be the result of two distinct processes: (1) A coherent scattering process, i.e. diffraction, in individual particles (density inhomogeneities) as described by the small-angle scattering theory (Glatter and Kratky 1982). For such scattering to occur within the angular range where it is termed USAXS, particles wider that a certain size (about 1 μm for most ABI setups) are required, as well as incident beams with coherence length wider than the particle size. (2) A process of multiple refractions through several particles (Muehleman et al. 2006). In this latter case, the amplitude of scattering does not depend on particle size. It depends basically on the number of particles along the beam path, i.e., the thickness of the imaged tissue (Heitner 2005). Therefore, coherent scattering (the first process) is the only scattering process able to provide the desired subpixel information, and it is the dominant process in thin samples, such as those investigated in the present study.

Any given scattering process is characterized by a reciprocal law, describing an inverse relationship between particle size and scattering angle (Glatter and Kratky 1982). For electron density inhomogeneities on a length scale R, this law also applies provided that the angular spreading of the scattered radiation of wavelength λ is roughly proportional to λ/R. In more specific terms, a statistical intensity distribution $\Gamma(\Delta\theta)$ can be assigned to each particular kind of inhomogeneity to describe the process as a function of the scattering angle $\Delta\theta$ from the incident beam direction. The angular spreading on a given scattering plane can hence be characterized by the quantity

$$\sigma_u^2 = \int_{-\alpha}^{+\alpha} (\Delta\theta)^2 \Gamma(\Delta\theta) \mathrm{d}\Delta\theta = \left[\frac{\lambda C_\Gamma(\alpha)}{R}\right]^2, \quad (1)$$

which is the standard deviation of the statistical distribution. $C_\Gamma(\alpha)$ is constant for nontruncated integrals, i.e., when $\alpha \gg \sigma_u$. From the general theory of small-angle scattering of X-rays, it is well known that the central region of the scattering curves is not related to the shape and symmetry of the scattering centers as long as they have the same radius of gyration R_g (as usually obtained from Guinier Law in a conventional SAXS experiment) (Glatter and Kratky 1982). Since σ_u is also essentially determined by the central region of the curves, its value is practically independent of $\Gamma(\Delta\theta)$ except for very anisometric scattering centers such as those with pronounced disc- or rod-like shapes. Then, within the Guinier approximation of the scattering curves $\Gamma(\Delta\theta) = a\pi^{-1/2}\exp\left(-a^2\Delta\theta^2\right)$ where $a = 2\pi R_g/\lambda\sqrt{3}$, which provides $\sigma_u = \lambda\sqrt{1.5}/2\pi R_g$. To quantify the size of the scattering centers, i.e., the length scale of subpixel density fluctuation in the samples, we have used the average spherical radius instead of R_g and hence $C_\Gamma \approx 1/4$ in Eq. 1.

Typical ABI setups require a parallel monochromatic beam and an analyzer crystal placed between the sample and the imaging detector. Under the conditions that photons exiting the object plane at a given point are scattered in the vertical plane, i.e., the diffraction plane of the analyzer crystal, in keeping with $\Gamma(\Delta\theta)$ and that each pixel in the detector is collecting all such photons (Rigon et al. 2007), the USAXS images comprise the values of σ_u as given in Eq. 1. In the statistical algorithm used to process multiple images from ABI data (Pagot et al. 2003), two rocking curves (RCs) of the analyzer crystal have to be

Table 1 Experimental ABI setups for the *hkl* analyzer reflection, X-ray energy (E), experimental (W_e) and theoretical (W_t) FWHM of the RC (Zhong et al. 2000), angular range $2w$ centered in the RC for image acquisition in increments of $d\theta$, and average maximum number of counts per pixel N_m acquired during the *reference* RC

Setup (label)	*hkl*	E (keV)	W_e/W_t (μrad)	$2w$ (μrad)	$d\theta$ (μrad)	N_m (counts)
A333E30	333	30	1.9/2.10	30	0.5	14,856
A333E52	333	52	1.3/1.29	16	0.4	11,545
A111E52	111	52	6.3/6.30	40	1.0	31,498

recorded on each pixel: one with the sample, the *object* RC, and another without the sample, the *reference* RC. Any difference in the standard deviations σ_{obj} and σ_{ref} of these RCs is directly related to the amount of USAXS on a given pixel since $\sigma_u = \left(\sigma_{obj}^2 - \sigma_{ref}^2\right)^{1/2}$, as previously described in detail elsewhere (Pagot et al. 2003). From the reciprocal law summarized in Eq. 1, the inaccuracy in determining the value of R on each pixel is given by

$$\Delta R/R = 8(R/\lambda)^2\sqrt{\left(\Delta\sigma_{obj}^2\right)^2 + \left(\Delta\sigma_{ref}^2\right)^2} \quad (2)$$

It is calculated by using simple error propagation theory for uncertainties $\Delta\sigma_{obj}^2$ and $\Delta\sigma_{ref}^2$ in the square values of the standard deviations. Both uncertainties, in turn, are estimated by propagating in the equations of σ_{obj}^2 and σ_{ref}^2 the statistical noise, $\pm\sqrt{N(\theta_n)}$ of radiation counting in the RCs where $N(\theta_n)$ is the number of counts in a pixel for the angular setting θ_n of the analyzer crystal.

X-ray measurements were performed at station X15A of the synchrotron light source (NSLS) in the Brookhaven National Laboratory. The two-bounce Si(111) monochromator of the beamline was set to nondispersive configuration with the Si(111) crystal analyzer in all experimental setups used. Experimental details are summarized in Table 1. The pixel size of the imaging detector system was 30 μm, and the estimated transversal coherence length of the beam was about 8 μm. The samples were prepared by surgery, which consisted of creating two 4-mm-diameter defects in the rat calvaria. One defect was filled with synthetic β-TCP calcium-phosphate (CP) grafting material (Synthograft, Bicon, Boston, MA, USA) and the other was left filled with the blood clot (control). The rats were sacrificed at 4 weeks after surgery, and the samples were maintained in 70% ethanol until tested.

General aspects of the samples were depicted via the refraction image shown in Fig. 1a, including CP-filled defect, control defect, CP-bone integration zone (IZ), and zone of naturally grown bone (NGB) since surgery. Scattering centers in the region of interest, embracing both defects, were evidenced by processing a differential absorption image (Pagot et al. 2003; Fig. 1b). In addition to an enhanced scattering at the CP-filled defect, scattering at the NGB zone could also be observed. A computed tomography slice of the sample (Fig. 1c) provides information on the actual thickness of both defects.

Subpixel spatial resolution was then investigated in two steps: (1) R images were processed from ordinary USAXS images by using the relationship $R = 0.25\lambda/\sigma_u$ (Eq. 1) and (2) graphical analysis was conducted of the statistical frequency of the values of $\Delta R/R$ (Eq. 2) and R on the pixels of a given image, leading to two-dimensional histograms. Examples of both types of results, R images and histograms, are shown in Fig. 2 for the area selected in Fig. 1b and for the three ABI setups in Table 1. Since the inaccuracy $\Delta R/R$ in the spatial resolution is proportional to λ^{-2}, or equivalently to E^2, it is not surprising that only the setup configured at lower energy, i.e., the A333E30 setup, was able to resolve

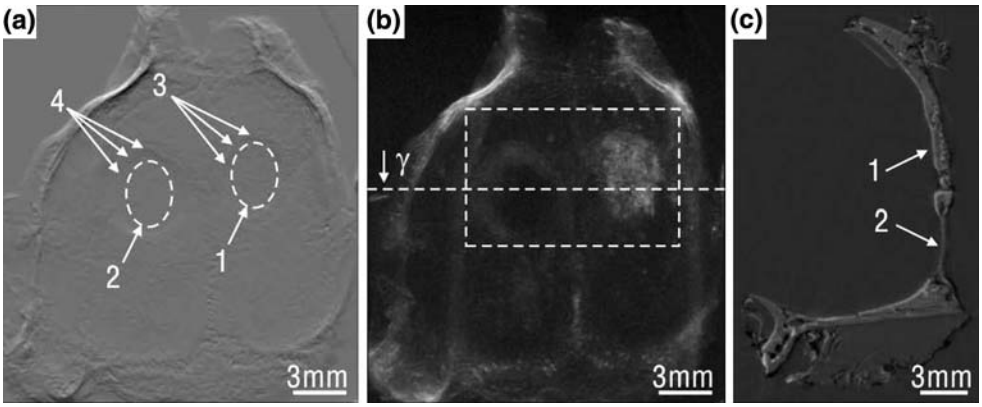

Fig. 1 Multiple image radiography of rat calvaria: **a** refraction image and **b** differential absorption (scattering) image. *Dashed circles* denote the CP-filled (*1*) and blood clot-filled (*2*) defects. CP-bone integration zone (*3*) and zone of thick naturally grown bone (NGB, *4*) since surgery are visible. **c** Two-dimensional computed tomography processed at position γ (*dashed line* in **b**), and analyzer setting at the slope of its RC. *1* CP-filled, *2* thin NGB. Experimental setup: A111E52

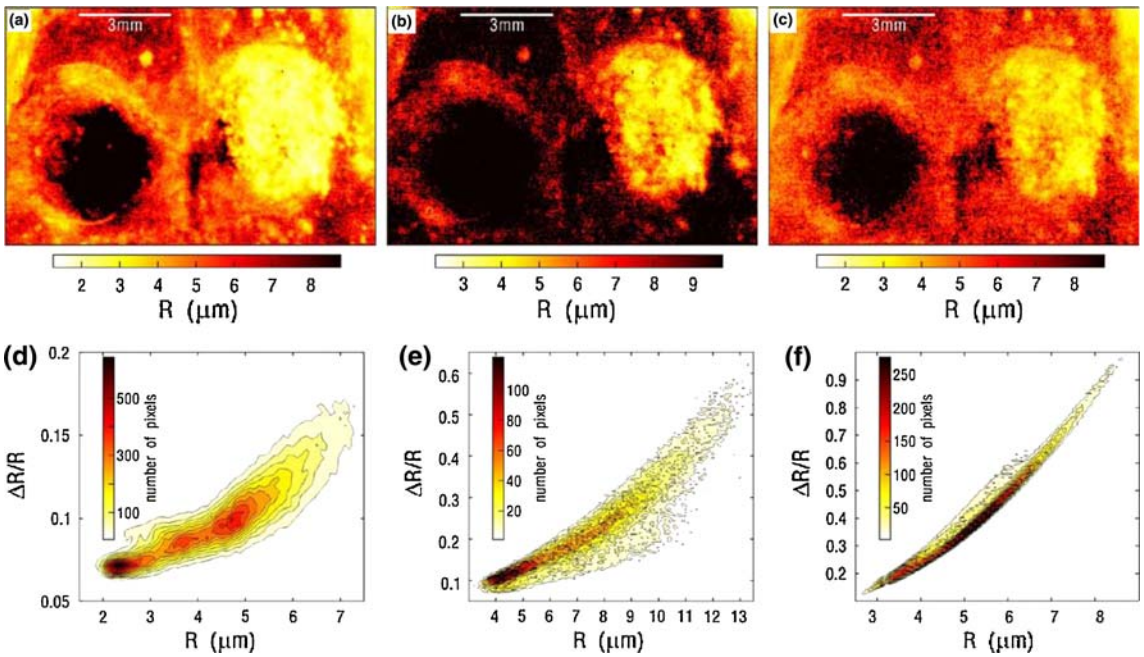

Fig. 2 **a**, **b**, **c** R images and **d**, **e**, **f** their respective accuracy, $\Delta R/R$, for three experimental setups: **a**, **d** A333E30; **b**, **e** A333E52; and **c**, **f** A111E52. Imaged area of 257 × 401 pixels (Fig. 1b)

the presence of distinct R values in the imaged area, as presented in Fig. 2d. At higher energy, $E = 52$ keV, such good resolution could not be observed in Fig. 2e and f, even for the configuration A333E52, which had the narrowest analyzer RC. Due to the limited range of $2w$ of the RCs, systematic errors arise with small values of R. We attempted to minimize these errors by computing $C_\Gamma(\alpha = w)$ using Eq. 1 within the spherical particle approximation for $\Gamma(\Delta\theta)$. Without correction, the discrepancy in the minimum observed R values in the A333E52 and A111E52 setups with respect to A333E30 would be more pronounced. Moreover, all resolved Rs in Fig. 2d are smaller than or close to 4 μm, which is half the estimated value of the X-ray beam coherence length. This is a necessary condition for coherent scattering. Improving the X-ray optics to increase the beam coherence length may not be useful in characterizing the presence of wider Rs because, according to Eq. 2, the inaccuracy $\Delta R/R$ is also proportional to R^2.

Evaluation of spatial resolution on the CP-filled defects was carried out on other samples, as shown in Fig. 3, but only for the A333E30 setup (Table 1). Higher definition of specific regions of the samples can be observed for this setup, for instance the NGB interface with the original calvaria bone as seen in Fig. 2a. As a general result for all samples, the texture (or roughness) of the original calvaria bone provided Rs of about 4.5–5.0 μm. In the NGB zone, it decreased to 3.8 μm, and in the thin NGB region it was undetectable (Fig. 2a). At the CP-filled defects, two particle size distributions (radius) were identified at $R = 1.8$ and 2.2 μm. In most cases in Fig. 3, both sizes were observed along with the occurrence of even smaller sizes ($R < 1.5$ μm) on a few pixels at the central area of the grafted material (white spots in Figs. 2a, 3a–c). A granular aspect of the β-TCP grafting materials on the order of 0.1 mm in diameter was also observed; however, the granules were scattered as compact aggregates of smaller grains with diameter ranging from $2R = 2$–3 μm (white spots) to about $2R = 4.0 \pm 0.4$ μm somewhat uniformly over the rest of the grafted area. Such a grain size gradient across the filled defects is indicative that the substance responsible for the thin NGB in the control defect is able to penetrate into the β-TCP granules along with apposition in the outer surface of the grafting material, wrapping up the tiny grains and promoting their growth by more than 1 μm in diameter during the first month after surgery.

In conclusion, within appropriated ABI setup configurations, subpixel inhomogeneities can be resolved. In the case of calcium phosphate (β-TCP) grafting materials, the A333E30 setup has allowed us to map over the extent of the imaged areas particles as wide as 5 μm in radius and with an accuracy of about ±0.2 μm, which is more than 100 times smaller than the used pixel size. The extracted information on each pixel was equivalent to the radius of gyration obtained via SAXS experiments with a microbeam the size of the pixel. Analysis of spatial resolution, i.e., histograms as in Fig. 2d, is necessary to extract quantitative information in studies intended to monitor changes in the size of the particles (scattering centers). For instance, evidence of gradients in the bone ingrowth process over the extent of CP-filled defects could be detected

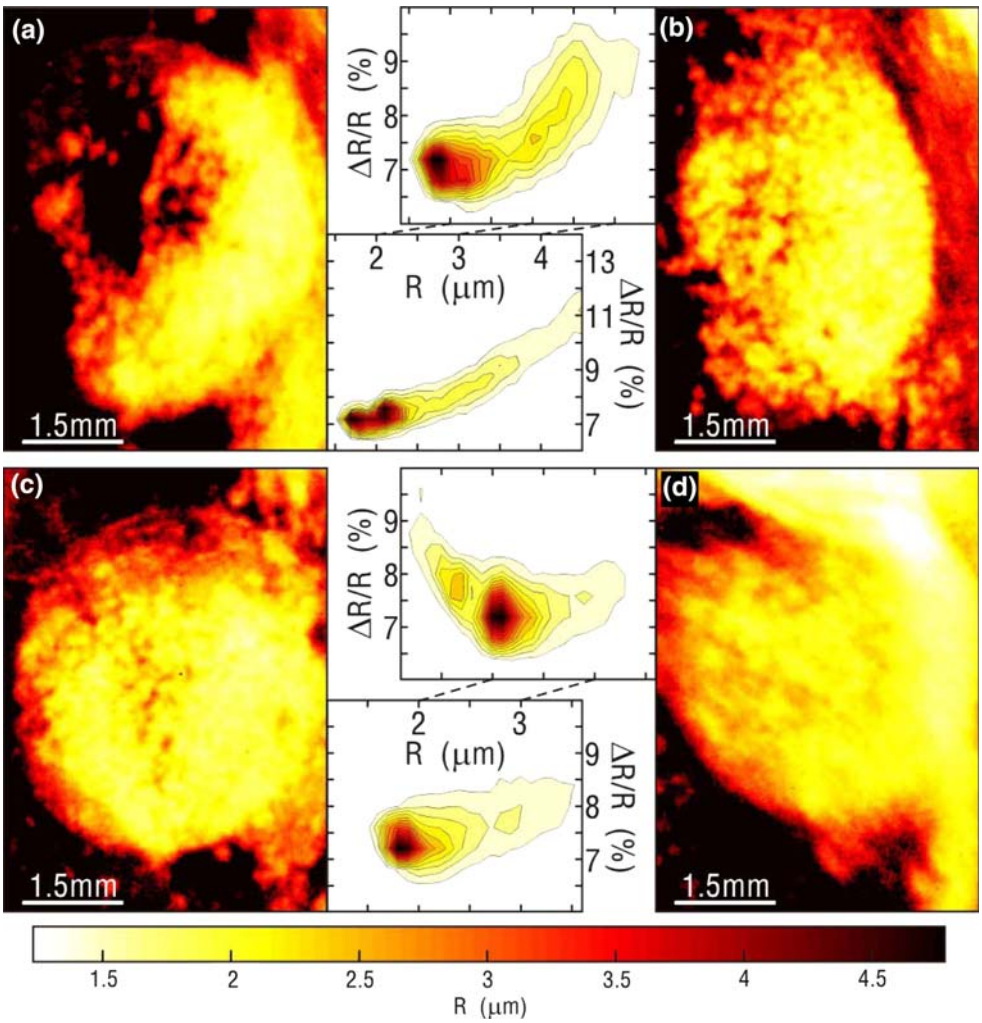

Fig. 3 *R* images of CP-filled defects from four different samples (**a**–**d**). Radius accuracy distribution maps are given beside each corresponding image. Experimental setup: A333E30

in the present experiment. The procedure described here is suitable to probing inhomogeneities at a length scale of a few microns and in relatively thin tissues where multiple refraction/scattering processes are negligible, such as ocular tissues, cancerous tissues, cartilages, and others.

Acknowledgments The authors gratefully acknowledge Z. Zhong for valuable discussions and Dean Connor Jr. for the expert technical assistance. Research was supported by the Brazilian agency FAPESP and CNPq. Use of the X15A beamline was supported by the U.S. Department of Energy contract no. DE-AC02-98CH10886 and by NIH grant R01 AR48292.

References

Antunes A, Safatle AMV, Barros PSM, Morelhão SL (2006) Med Phys 33:2338
Bonse U, Hart M (1966) Z Physics 189:151
Coan P, Mollenhauer J, Wagner A, Muehleman C, Bravin A (2008) Eur J Radiol 68:S41
Davis TJ, Gao D, Gureyev TE, Stevenson AW, Wilkins SW (1995) Nature 373:595
Foerster E, Goetz K, Zaumseil P (1980) Krist Tech 15:937
Glatter O, Kratky O (eds) (1982) Small angle scattering of X-rays. Academic Press, London
Heitner GH (2005) Ph.D. Thesis, Universität Siegen, Siegen, Germany
Hönnicke MG, Kakuno EM, Kellerman G, Mazzaro I, Abler D, Cusatis C (2008) Optics Express 16:9284
LeGeros RZ (1991) Monogr Oral Sci 15:1
Lemons JE (1996) Bone 19:S121
Levine L, Long GG (2004) J Appl Cryst 37:757
Muehleman C, Li J, Zhong Z, Brankov JG, Wernick MN (2006) J Anat 208:115
Pagot E, Cloetens P, Fiedler S, Bravin A, Coan P, Baruchel J, Hartwig J, Thomlinson W (2003) Appl Phys Lett 82:3421
Pfeifer F, Weitkamp T, Bunk O, David C (2006) Nat Phys 2:258
Pisano ED, Johnston RE, Chapman D, Geradts J, Iacocca MV, Livasy CA, Washburn DB, Sayers DE, Zhong Z, Kiss MZ et al (2000) Radiology 214:895
Rigon L, Arfelli F, Menk R-H (2007) Appl Phys Lett 90:114102
Wagner A, Sachse A, Keller M, Aurich M, Wetzel W-D, Hortschansky P, Schmuck K, Lohmann M, Reime B, Metge J et al (2006) Phys Med Biol 51:1313
Westneat MW, Betz O, Blob RW, Fezzaa K, Cooper WJ, Lee W-K (2003) Science 299:558
Wilkins W, Gureyev TE, Gao D, Pogany A, Stevenson A (1996) Nature 384:335
Zhong Z, Thomlinson W, Chapman D, Sayers D (2000) Nucl Instrum Meth A 450:556